

Ferroelectric domain scaling and electronic properties in ultrathin BiFeO₃ films on vicinal substrates

Vilas Shelke,^{1*} Dipanjan Mazumdar,¹ Sergey Faleev¹, Oleg Mryasov^{1,2}, Stephen Jesse,³ Sergei Kalinin,³ Arthur Baddorf,³ and Arunava Gupta¹

¹Center for Materials for Information Technology, University of Alabama, Tuscaloosa, AL, 35487 USA

²Department of Physics, University of Alabama, Tuscaloosa, AL, 35487 USA

³Center for Nanophase Materials Sciences, Oak Ridge National Laboratory, Oak Ridge, TN 37831 USA

Abstract

We report electrically switchable polarization and ferroelectric domain scaling over a thickness range of 5-100 nm in BiFeO₃ films deposited on [110] vicinal substrates. The BiFeO₃ films of variable thickness were deposited with SrRuO₃ bottom layer using pulsed laser deposition technique. These films have fractal domain patterns and the domain width scales closely with the square root of film thickness, in accordance with the Landau-Lifschitz-Kittle (LLK) law. The Switching Spectroscopy Piezo-response Force Microscopy provides clear evidence for the ferroelectric switching behavior in all the films. Local tunneling current vs voltage measurements performed on the 5nm film reveal a high potential energy barrier for electrons. We explain this as possibly due to a high attenuation constant for tunneling electrons as indicated by *ab-initio* band structure calculations. Using the Quasi-particle Self-consistent GW (QSGW) theory, we obtain band gap values of 3.3 eV and 2.31 eV for the rhombohedral and tetragonal BFO structures respectively.

PACS Numbers: 77.55.Nv, 77.80.Dj, 77.80.Fm, 81.15.Fg, 68.37.ps

* Corresponding author, present address- Department of Physics, Barkatullah University, Bhopal- 462 026 INDIA; e mail- drshelke@gmail.com

I. INTRODUCTION

In the era of miniaturization and power conservation each quantum of power and size matters a lot. The particularly influenced are the information storage devices. The topical trend is the spin polarized tunneling with ferroelectric control, which relies on zero current gate controlled operation with low power dissipation.¹ The use of electrically switchable ferroelectric tunnel junctions for nonvolatile memory devices^{2,3} is providing an impetus for extensive study on ultrathin ferroelectric films⁴⁻⁷. In this context, BiFeO₃ is a material with huge potential mainly due to its multiferroic character, which provides ability to switch effectively by electric or magnetic field.⁸ Intriguingly, it may also turn out to be power saving material with fundamentally different photovoltaic effect.^{9,10} Therefore, deposition and observation of ferroelectricity in ultrathin BiFeO₃ films is of current research interest.

The recent studies on BiFeO₃ (BFO) thin films are guided by two aspects viz. tetragonality and vicinality. The BFO films deposited on large lattice mismatched substrates like LaAlO₃ show monoclinically distorted tetragonal structure.^{11,12} The stabilization of pure tetragonal phase remains elusive although the theoretical calculations suggest strain¹³ and electric field¹⁴ induced phase stabilization or transition. We have reported ferroelectric behavior of strain relaxed BiFeO₃ thin films on lattice mismatched substrates¹⁵ and have also pursued the tetragonality issue for the fundamental understanding using Piezo-response Force Microscopy (PFM) and polarized Raman Spectroscopy techniques.^{16,17} On the other hand, deposition of BFO films on vicinal substrates can assist engineering of ferroelectric domain structure.^{18,19} Such films have two domain variants as compared to four domain variants observed in thin films deposited on plain substrates. As a consequence the ferroelectric switching is better on vicinal substrates. Our study on BFO films deposited on SrTiO₃ substrates having 4⁰

miscut along [110] direction revealed higher polarization value and significantly reduced coercive field.²⁰ It is clear that the domain structure plays a vital role in governing the technologically important parameters like polarization and coercive field.

In BFO films, the ferroelectric domains are large in dimensions and are stripe or fractal types.⁸ Generally, the domains follow the Landau, Lifshitz and Kittle (LLK) law wherein the domain width scales with the square root of film thickness.²¹ However, deviation from this law is recently reported in very thin BFO films deposited on plain SrTiO₃ substrates.²² Therefore, from fundamental and application point of view, it is pertinent to study the ferroelectric behavior and domain structure in ultrathin films deposited on vicinal substrates. For the present work, we deposited 5-100 nm thickness BFO films on SrTiO₃ substrates with 4° miscut along [110] direction. We confirmed the structural quality of the films using X-ray diffraction technique. The fractal domains with variable dimensions were observed using Piezo-response Force Microscopy. We tried to fit the domain size variation with the film thickness in accordance with LLK law. We also provide unambiguous evidence for the ferroelectricity in ultra-thin (up to 5 nm) BFO films using advanced Switching Spectroscopy Piezo-response Force Microscopy (SSPFM) technique. In addition, we have investigated the local tunneling properties of rhombohedral BFO as a spintronic barrier and found a relatively high potential energy barrier height for tunnel electrons both experimentally and from *ab-initio* methods. The Quasi-particle GW approximation, which is known to substantially improve the band-gap problem of DFT, gave band gap values of 3.3 eV and 2.31 eV for the rhombohedral and tetragonal BFO structures respectively.

II. EXPERIMENTAL

We have deposited BiFeO₃ (BFO) thin films of variable thickness in the range 5-100 nm on (100) SrTiO₃ substrates with 4° miscut along [110] direction. The BFO films with SrRuO₃ (SRO) bottom layer were deposited sequentially using pulsed laser deposition method.²³ The crystalline quality and out of plane lattice parameters were determined using X-ray Diffraction (X'pert Pro. Panalytical) with CuK_α radiation. The surface topography and domain structure were revealed using Atomic and Piezo-response Force Microscopy under ambient conditions. For this purpose, commercial Scanning Probe Microscope (Cypher, Asylum Research) equipped with Pt coated conducting tip (AC240TM, Olympus) was operated at the resonance frequency around 260 kHz and ac bias amplitude of 2V. The same set up was augmented to perform advanced Switching Spectroscopy Piezo-response Force Microscopy (SS-PFM) measurements.^{24,25} We used 25 x 25 grid on 2 μm x 2 μm scan area to map the local polarization switching with variable tip bias between +10 V and -10 V. Similarly, we measured local current vs voltage (I-V) characteristics at intermediate voltage of ± 2 V. Details about the *ab-initio* methods are described later in an appropriate section.

III. RESULTS AND DISCUSSION

A. Structural Analysis

The X-ray diffraction patterns (θ -2 θ scan) of 100, 50, 20 and 10 nm BFO films deposited with 40 nm SRO bottom layer on STO substrates with 4° miscut along [110] direction are shown in Fig. 1 (a). The inset shows clearly distinguishable (100) peaks. The highly oriented textured growth of the films is evident from the appearance of (*00l*) peaks. The representative omega and phi scans shown in Fig. 1 (b) and (c) clearly reveal the crystalline quality and epitaxial nature of these films. The full width half maxima

(FWHM) values for the omega scan were around 0.04° and the phi scan exhibited four-fold symmetry. The out of plane lattice parameters determined from XRD data were 4.01, 4.05, 4.06, and 4.08 \AA for the 100, 50, 20 and 10 nm thickness films. The bulk value for the pseudo-cubic lattice parameter is 3.96 \AA . However, the substrate induced in-plane compression of unit cells causes out of plane elongation. A variation in lattice parameter has been reported with the substrates^{11,26}, with film thickness²⁷ and also with operating oxygen pressure²⁸. Our films seem somewhat constrained with reducing thickness, which is in agreement with the reported behavior for other miscut substrates.¹⁸ On plain substrates, the change in lattice parameters for the BFO films below 100 nm thickness is quite small.^{5,27}

B. Ferroelectric domain scaling and switching behavior

The surface topography scans of $2 \mu\text{m} \times 2 \mu\text{m}$ area of the 100, 50, 20, 10 and 5 nm thickness BFO films are shown in Fig. 2 (a)-(e) respectively. In general BFO films are known to grow in 3-D island growth mode.¹⁸ However, step flow growth mode has been reported on orthorhombic DyScO₃ substrates²⁹, on the miscut substrates^{18,26} and possibly with growth under optimized oxygen pressure²⁸. The parallel steps with larger width resulting from step bunching were reported on the substrates with 4° miscut along [100] direction.^{18,26} On the other hand, when miscut angle is along [110] direction, as in the present case, the steps have saw-tooth pattern.²⁰ The parallel steps promote nanowire kind of growth along the steps or perpendicular to miscut direction. The saw-tooth steps may promote nanoparticle kind of growth on the triangular steps. Further, the step bunching is possible making the saw-tooth patterns more washed out. In Fig. 2 (a)-(e) the topographical patterns show traces of saw-tooth step flow growth. They are similar except the grain size becomes smaller with reducing thickness of the films.

The evolution of ferroelectric domains with variant film thickness, recorded through vertical PFM, is shown in Fig. 2 (f)-(j). The black and white contrasts in these images indicate polarization components pointing in down and up directions respectively. It has been documented that the BFO films have four and two polarization variants when deposited on exact and [100] vicinal substrates respectively.^{18,26} The domains have large size and stripe patterns running perpendicular to the vicinal direction. Jang *et al* attributed such pattern formation to the relaxation of elastic-strain energy of the films on step surfaces without the necessity of two additional domain variants.¹⁸ However, the vicinality along [110] direction yields saw-tooth step pattern, which may break the symmetry of stripe domains. It results in two variant domains with pattern intermediate of stripe and fractal. Such domains can have double advantages viz. better polarization due to two variants and better switchability resulting from step-edge dislocations.²⁰

An important feature of these domain patterns is the systematic reduction of domain size with the thickness. The contrast patterns with reducing dimensions were seen up to 10 nm thickness films. The 5 nm thickness film did not show the signature of domain formation probably due to crosstalk interference. On plain STO substrates, Daumont *et. al.*,⁵ could not detect the contrast in 12 nm thickness BFO films whereas Catalan *et. al.*,²² reported fractal domains up to 7 nm thickness films. They also reported the domain periodicity measured by Fourier analysis or by simply counting the number of domains across a straight segment. The average domain size departed from the classic LLK square root dependence on film thickness with the scaling exponent $\gamma = 0.59$. Alternatively, Zhao *et. al.*, proposed square dependence of domain period on thickness for PbTiO₃ ultrathin films.³⁰ The variation of domain width as a function of film thickness for the BFO films on vicinal substrates is shown in Fig. 3. The curve fitting to the law $w = Ad^\gamma$, where w is the average domain width and d is the film thickness, gave the scaling

exponent value $\gamma = 0.49 \pm 0.05$, which is very close to the LLK value of 0.5.²¹ However, it is smaller than the value 0.59 reported by Catalan *et. al.*,²² for the BFO thin films on plain substrate. This difference may be the attribute of substrate vicinality. On plain substrate the domains in thick film are larger with four polarization variants. The reduction of film thickness can cause rapid reduction in domain size making the scaling exponent greater than 0.5. On the other hand, use of [110] vicinal substrates yield mostly fractal domains due to saw-tooth pattern of steps. The specific reason for fractality of domains is not very clear. However, low crystal anisotropy and pinning defects are responsible for their appearance.⁸ The terraces, steps, kinks, etc on [110] vicinal substrates can provide ample sites for the domain formations. Therefore, the domain size reduction with thickness may not be as rapid as in the case of plain substrates. Consequently, the scaling exponent is lower than 0.5.

There are quite a few riddles associated with the fundamental limit of ferroelectricity. In principle, the charge polarization occurs through the non-centrosymmetric arrangement of the atoms in perovskite unit cell. However, the celebrated concept of ‘dead layers’ in dielectric thin films indicate that there is a limit for the occurrence of polarization.^{31,32} Stengel *et. al.*,³³ also proposed through the first-principle calculations an innovative concept of positive dead layer, which may actually enhance the ferroelectricity at the interface. The issue was complicate till the availability of reliable experimental technique to measure the polarization in ultrathin films, where high leakage current hampers the macroscopic measurements. The recent advancements in Scanning Probe Microscopy provided an effective tool to characterize localized ferroelectric response.^{24,25} The electrical switching behavior has been reported in 1 nm BaTiO₃,² 30 nm PbZrTiO₃,³ and 40 nm BiFeO₃³⁴ films using PFM switching technique. The switching behavior of our films is shown in Fig. 4 (a)-(c). The characteristic butterfly

loops were observed in amplitude signals of all the BFO films including the 5 nm thickness film (Fig. 4 a). Fig. 4 (b) shows the phase signal indicative of clear switching behavior. The collective piezo-response shown in Fig. 4 (c) also confirms that clear and complete polarization switching can be accomplished within the bias of ± 10 V. It gives an unambiguous evidence for the occurrence of ferroelectricity in BFO films as thin as 5 nm deposited on vicinal substrates. However, it is difficult to quantify the magnitude of polarization and coercive field from SS-PFM data alone.²⁵ Nevertheless, the macroscopic measurements on thick films indicated that the effective switching of BiFeO₃ films on [110] vicinal substrates can be accomplished with lower voltage or reduced coercive field.²⁰ Therefore, the 5 nm BiFeO₃ films deposited on [110] vicinal substrate may satisfy the dimensional constraints for tunneling as well as the existence of switchable ferroelectricity. Recently, Maksymovych *et. al.*,³ have reported the simultaneous measurement of switchable polarization and local conductance in 30 nm tunnel barrier of PZT film.

C. Transport properties

The unique combination of magnetic and ferroelectric properties has stimulated research on the current perpendicular to the plane heterostructures with BFO thin films for new electronic functionalities³⁵. These results motivated further work on understanding tunneling properties of BFO films for spintronics applications as a multiferroic tunnel barrier. Here, we report preliminary investigation into the tunneling properties of BiFeO₃ ultrathin films performed through local current vs voltage (I-V) measurements using conducting scanning probe tip of AFM. In Fig. 5 (a), we have plotted the current density (J) vs voltage (V) measured for the 5nm BFO film with voltage bias range of ± 2 V. Voltage was applied to the probe tip and current out of the sample was measured with the

help of current amplifier (with a maximum gain of 10^9). The non-linear behavior, characteristic of tunneling, was fitted to the Simmons phenomenological model used widely to estimate tunnel barrier properties.³⁶ The schematic diagram of the model implementation is shown in Fig. 5(b). Here, tunneling through a trapezoidal barrier is considered with similar metal electrodes on either side of the barrier, and the current density for intermediate voltage bias is given by,

$$J = \left(\frac{\gamma\sqrt{\phi}}{d} \right) \exp(-A\sqrt{\phi}) (V + \sigma V^3) \quad (1)$$

where, $\gamma = e\sqrt{2m} / 4b\pi^2 (h/2\pi)^2$, $A = 4\pi d\sqrt{2m} / h$, $\sigma = \frac{(Ae)^2}{96\phi d^2} - \frac{Ae^2}{32d\phi^{\frac{3}{2}}}$
 $b = 23/24$, $m =$ free electronic mass $= 9.31 \times 10^{-31}$ kg, $h =$ Planck's constant $= 6.63 \times 10^{-34}$ J.s, $e =$ electronic charge $= 1.603 \times 10^{-19}$ C, d is the effective barrier thickness, and ϕ is the effective mean barrier height.

As equation 1 shows, tunneling is linear in the low voltage bias regime and non-linearity is captured in the cubic term at higher voltages. The measured current density for the 5 nm film is extremely low and implies extremely high resistance-area (RA) product factor for BFO based spintronic devices. Such high resistance values are consistent with existing reports.³⁷ An asymmetry observed in the experimental curve and deviation of the curve from the Simmons fit can be attributed to dissimilar electrodes in the experimental setup. With a tip radius of ~ 10 nm, and barrier width of 5nm we obtain an effective barrier height of 4.15 eV, substantially higher than the half of the experimental band gap $E_g/2=1.4\text{eV}$ ³⁸ (we assume here that the Fermi energy of electrodes is aligned in the middle of the BFO band gap). Below we discuss possible mechanism of such tunneling behavior on the basis of electronic structure calculations.

D. Electronic properties

Indeed, in a magnetic tunnel junction device, the resistance as a function of barrier thickness is empirically given by $R=R_0e^{2\gamma d}$, where d is barrier thickness and γ is the attenuation (decay) constant which depends on the electronic structure of barrier material. For direct band-gap materials with free electron-like bands in the vicinity of the band gap the attenuation constant could be expressed in terms of the effective mass of the electronic states at the top of valence band (m_v^*) and bottom of the conduction band (m_c^*). In particular, Butler *et al.*³⁹ modeled the decay rates for free electron-like bands of MgO with Δ_1 -symmetry as

$$\gamma = \left(\frac{\hbar^2}{2m_v^*(E - E_v)} + \frac{\hbar^2}{2m_c^*(E_c - E)} \right)^{-1/2} \quad (2)$$

Here E_v and E_c are the energies of the valence and conduction band edges and E is the energy of the propagating electrons inside the band gap. Note that at high symmetry points in surface Brillouin zone in a plane perpendicular to current direction the evanescent states emerging from electrode bands with different symmetry could decay at different rates giving rise to a symmetry filtering effects as discussed in details for the case of Fe/MgO/Fe.⁴⁰ On the other hand, for thick enough barriers the electrode evanescent states (with wave vectors in surface Brillouin zone that do not possess high symmetry) will generally decay with lowest possible γ available in the barrier at a given wave vector.

An important consequence of Eq. (2) is that the average potential barrier height can be dramatically different from the band gap value. For instance, the average potential barrier height for Fe/MgO/Fe measured experimentally is 0.4eV, whereas from simplistic band gap considerations it ought to be 3.7 eV, half the band gap of bulk MgO.⁴⁰ It is well established by now that such low effective tunneling potentials observed in Fe/MgO/Fe

are due to small effective masses at band edges of MgO and not due to extrinsic effects such as oxygen vacancies. Below we investigate how these two factors, band gap and effective masses at the band edges contribute to an effective tunneling barrier in the case of epitaxial high quality BiFeO₃ films.

To account for both of these factors on the level of accuracy beyond traditional Density Functional Theory (DFT), we employ highly accurate many body perturbation theory or Quasiparticle Self-Consistent GW (QSGW) theory.⁴¹ More specifically we used scaled version⁴² of the QSGW method, namely, we scale the difference of the self-energy and LDA exchange-correlation potential by a factor 0.8, $(\Sigma - V_{xc}) \rightarrow 0.8(\Sigma - V_{xc})$, that effectively takes into account renormalization of the polarization operator due to the electron-hole interaction. It is expected that band gaps within QSGW theory are somewhat overestimated due to electron-hole (exitonic) interaction effects, which are not included within the original GW theory formulation. Earlier, it has been shown that exitonic effects (additional ladder diagrams for polarization operator) account for most of the remaining errors in QSGW predicted band gaps.⁴³ Fortunately, it was shown⁴² that a simple scaling procedure with *universal* scaling factor 0.8 accounts for these exitonic and significantly improves QSGW results for band gaps. Note that self-consistency enabled by QSGW method is expected to be important for calculating band gaps of transition metal based oxides.⁴¹ Other important property contributing directly to effective tunneling barrier such as work function in case of transition metals and compounds also require self-consistent treatment⁴⁴. In Fig. 6 we compare electronic structure calculated within this many-body perturbation theory in comparison with earlier results obtained within the mean field type LDA/DFT or LDA+U theory [see Ref 45, for example]. The many-body nature of the QSGW method enables predictive calculations⁴¹⁻⁴⁴ of electronic and magnetic properties of materials with higher accuracy compared to LDA/DFT. The

QSGW (solid) and LDA (dashed) electronic bands are presented in Fig. 6. The LDA electronic bands agree fairly well with that of Neaton *et al.*⁴⁵ who reported an indirect BFO band gap with value between 0.5-1.9eV, depending on the U_{eff} parameter value (0-4eV). U_{eff} is an effective Coulomb correlation treated within the LDA+U theory as rather arbitrary adjustable parameter. It is worse of noting that LDA+U yields much smaller values of the band gap compared to experimental band gap (2.8 eV)³⁸ even for rather liberally chosen large values of the U_{eff} (U-J) effective Coulomb interaction parameter.

Significant difference of the electronic bands calculated within the QSGW and the LDA should be noted as manifestation of important electron correlation effects in this material system. The QSGW band gap of 3.3 eV is in good agreement with experimental BFO band gap of 2.8 eV. The LDA band gap is about 0.7 eV, significantly smaller than the reported experimental value due to well-known self-interaction problem of LDA/DFT. (Let us mention here that the value of the BFO band gap has been an important subject of discussion in the context of photo-voltaic properties of BFO.¹⁰) The conduction band minimum (CBM) falls at the same Z point in both methods, but the valence band maximum (VBM) is between the Z and Γ points in LDA while it is between F and Γ points in QSGW (there is also local maximum of QSGW valence bands between Z and L points that is very close to VBM). The effective masses are also different in LDA and QSGW. The effective mass at CBM (Z point) in direction of the BFO barrier growth, the Z-F direction, is $m_c^* = 2.2m$ in QSGW, while it is $m_c^* = 3.4m$ in LDA. Overall flatness of the bands, due to the *d* nature of Fe states, and corresponding high effective masses are in agreement with the high effective barrier height of 4.15 eV determined from the tunneling measurement as shown in Fig. 5 (b).

Here, we use calculated electronic structure for estimation of the effective barrier height that enters exponential factor in Eq. (1). We employ simple model of Eq. (2) for attenuation constant. Assuming that the Fermi energy of the electrode is aligned in the middle of the BFO band gap and using QSGW band gap $E_g = 3.3$ eV and effective mass at Z point (in Z-F direction) $m_c^* = 2.2m$, we obtain the QSGW effective barrier height as,

$$\varphi^{QSGW} = \frac{E_g m_c^*}{2m} = 3.63 eV \quad (3)$$

Here, we used the fact that the QSGW effective mass at the top of the valence band at Z point is much larger than m_c^* (QSGW band is essentially flat at Z). The value of $\varphi^{QSGW} = 3.63$ eV agrees rather well with experimental effective barrier height $\varphi = 4.15$ eV. Eq. (3) with LDA band gap $\varphi^{LDA} = 1.19$ eV, $E_g = 0.7$ eV, and effective mass $m_c^* = 3.4m$, gives LDA effective barrier height much less than the experimental value. Inspired by these results, we also calculated electronic band structure of the BFO tetragonal phase as shown in Fig. 6 (b). Detailed comparison between BFO phases and with experiments will be published elsewhere. Here, we would like just to highlight that $P4mm$ BFO with reported structure parameters^{13,46} has significantly smaller band gap of about 2.31 eV and electron mass at the G point in G-Z direction $m^* = 0.33m$ so that effective tunneling barrier analogous to the model of the Eq.1 can be estimated according to the Eq. (3) as $V_{eff} = 0.38$ eV. This result is encouraging as it indicates that for spintronics and solar cell applications, favorable band structure “engineering” could be possible with strain stabilized tetragonal phase of BFO.

IV CONCLUSION

We deposited SrRuO₃ bottom layered 5-100 nm thickness BiFeO₃ films on the vicinal SrTiO₃ substrates with 4° miscut along [110] direction. The choice of substrate was to yield two variant domain structures with better ferroelectric properties. The epitaxial and constrained films showed traces of saw-tooth step flow growth in topographical features. The Piezo-response Force Microscopy revealed two variant fractal domains. The domain width scaling with film thickness closely followed the KKL law. A clear switching was observed through Switching Spectroscopy Piezo-response Force Microscopy in all the films including the ultrathin 5 nm film. From local I-V measurements, we conclude BFO to be a high resistance barrier material with an effective barrier potential of over 4 eV.

In order to compare our experimental findings with theory we performed *ab initio* calculation of the band structure of BFO by using LDA and QSGW methods. Overall flatness of the bands (due to the *d* nature of Fe states) and corresponding large effective mass at CBM leads to a high attenuation constant for tunnel electrons in agreement with high effective barrier height derived from the tunneling measurement. Both the value of the QSGW band gap (3.3 eV) and effective barrier height (3.63 eV) agree rather well with experimentally measured band gap (2.8 eV) and effective barrier height (4.15 eV), while LDA significantly underestimate the band gap (0.7 eV) and effective barrier height (1.19 eV). We also employed QSGW theory for tetragonal phase of BFO and found band gap (2.31 eV), effective mass (0.33m) and effective tunneling barrier (0.38 eV) assuming defect free film, band alignment in the center of the band gap and AF (001) magnetic structure.

ACKNOWLEDGEMENT

This work was supported by ONR under Grant No. N00014-09-1-0119 and NSF NIRT under Grant No. CMS-0609377. A portion of this research was conducted at the Center for Nanophase Materials Sciences, which is sponsored at Oak Ridge National Laboratory by the Division of Scientific User Facilities, U.S. Department of Energy. OM and SF acknowledge the CNMS User computer support by Oak Ridge National Laboratory Division of Scientific User facilities, Office of Basic Energy Sciences, U.S. Department of Energy.

1. V. Garcia, M. Bibes, L. Bocher, S. Valencia, F. Kronast, A. Crassous, X. Moya, S. Enouz-Vedrenne, A. Gloter, D. Imhoff, C. Deranlot, N. D. Mathur, S. Fusil, K. Bouzehouane, and A. Barthelemy, *Science* **327**, 1106 (2010).
2. V. Garcia, S. Fusil, K. Bouzehouane, S. Enouz-Vedrenne, N. D. Mathur, A. Barthelemy, and M. Bibes, *Nature* **460**, 81 (2009).
3. P. Maksymovych, S. Jesse, P. Yu, R. Ramesh, A. P. Baddorf, and S. V. Kalinin, *Science* **324**, 1421 (2009).
4. D. A. Tenne, P. Turner, J. D. Schmidt, M. Biegalski, Y. L. Li, L. Q. Chen, A. Soukiassian, S. Trolrier-McKinstry, D. G. Schlom, X. X. Xi, D. D. Fong, P. H. Fuoss, J. A. Eastman, G. B. Stephenson, C. Thompson, and S. K. Streiffer, *Phys. Rev. Lett.* **103**, 177601 (2009).
5. C. J. M. Daumont, S. Farokhipoor, A. Ferri, J. C. Wojdel, J. Iniguez, B. J. Kooi, and B. Noheda, *Phys. Rev. B* **81**, 144115 (2010).
6. A. Crassous, V. Garcia, K. Bouzehouane, S. Fusil, A. H. G. Vlooswijk, G. Rispens, B. Noheda, M. Bibes, and A. Barthelemy, *Appl. Phys. Lett.* **96**, 042901 (2010).
7. A. Gruverman, D. Wu, H. Lu, Y. Wang, H. W. Jang, C. M. Folkman, M. Ye. Zhuravlev, D. Felker, M. Rzchowski, C.-B. Eom, and E. Y. Tsybal, *Nano Lett.* **9**, 3539 (2009).
8. G. Catalan and J. F. Scott, *Adv. Mater.* **21**, 2463 (2009).
9. T. Choi, S. Lee, Y. J. Choi, V. Kiryukhin, and S. W. Cheong, *Science* **324**, 63 (2009).
10. S. Y. Yang, J. Seidel, S. J. Byrnes, P. Shafer, C.-H. Yang, M. D. Rossell, P. Yu, Y.-H. Chu, J. F. Scott, J. W. Ager, L. W. Martin and R. Ramesh, *Nature Nanotechnol.* **5**, 143 (2010).
11. H. Bea, B. Dupe, S. Fusil, R. Mattana, E. Jacquet, B. Warot-Fonrose, F. Wilhelm, A. Rogalev, S. Petit, V. Cros, A. Anane, F. Petroff, K. Bouzehouane, G. Geneste, B.

- Dkhil, S. Lisenkov, I. Ponomareva, L. Bellaiche, M. Bibes, and A. Barthelemy, *Phys. Rev. Lett.* **102**, 217603 (2009).
- ¹² R. J. Zeches, M. D. Rossell, J. X. Zhang, A. J. Hatt, Q. He, C.-H. Yang, A. Kumar, C. H. Wang, A. Melville, C. Adamo, G. Sheng, Y.-H. Chu, J. F. Ihlefeld, R. Erni, C. Ederer, V. Gopalan, L. Q. Chen, D. G. Schlom, N. A. Spaldin, L. W. Martin, and R. Ramesh, *Science* **326**, 977 (2009).
- ¹³ A. J. Hatt, N. Spaldin, and C. Ederer, *Phys. Rev. B* **81**, 054109 (2010).
- ¹⁴ S. Lisenkov, D. Rahmedov and L. Bellaiche, *Phys. Rev. Lett.* **103**, 047204 (2009).
- ¹⁵ V. Shelke, G. Srinivasan, and A. Gupta, *Phys. Status Solidi RRL*, **4**, 79 (2010).
- ¹⁶ D. Mazumdar, V. Shelke, M. Iliev, S. Jesse, A. Kumar, S. V. Kalinin, A. P. Baddorf, and A. Gupta, *Nano Lett.* **10**, 2555 (2010).
- ¹⁷ M. N. Iliev, M. V. Abrashev, D. Mazumdar, V. Shelke, and A. Gupta, *Phys. Rev. B* **82**, 014107 (2010).
- ¹⁸ H. W. Jang, D. Ortiz, S. H. Baek, C. M. Folkman, R. R. Das, P. Shafer, Y. Chen, X. Pan, R. Ramesh, and C. B. Eom, *Adv. Mater.* **21**, 817 (2009).
- ¹⁹ Y. H. Chu, M. P. Cruz, C. H. Yang, L. W. Martin, P. L. Yang, J. X. Zhang, K. Lee, P. Yu, L. Q. Chen, and R. Ramesh, *Adv. Mater.* **19**, 2662 (2007).
- ²⁰ V. Shelke, D. Mazumdar, G. Srinivasan, A. Kumar, S. Jesse, S. V. Kalinin, A. P. Baddorf, and A. Gupta, *Adv. Mater.* under revision (2010).
- ²¹ C. Kittle, *Rev. Mod. Phys.* **21**, 541 (1949).
- ²² G. Catalan, H. Bea, S. Fusil, M. Bibes, P. Paruch, A. Barthelemy, and J. F. Scott, *Phys. Rev. Lett.* **100**, 027602 (2008).
- ²³ V. Shelke, V. N. Harshan, S. Kotru, and A. Gupta, *J. Appl. Phys.* **106**, 104114 (2009).
- ²⁴ S. Jesse, H. N. Lee, and S. V. Kalinin, *Rev. Sci. Instru.* **77**, 073702 (2006).

25. S. V. Kalinin, B. J. Rodriguez, A. Y. Borisevich, A. P. Baddorf, N. Balke, H. J. Chang, L.-Q. Chen, S. Choudhury, S. Jesse, P. Maksymovych, M. P. Nikiforov, and S. J. Pennycook, *Adv. Mater.* **22**, 314 (2010).
26. R. R. Das, D. M. Kim, S. H. Baek, C. B. Eom, F. Zavaliche, S. Y. Yang, R. Ramesh, Y. B. Chen, X. Q. Pan, X. Ke, M. S. Rzechowski, and S. K. Streiffer, *Appl. Phys. Lett.* **88**, 242904 (2006).
27. D. H. Kim, H. N. Lee, M. D. Biegalski, and H. M. Christen, *Appl. Phys. Lett.* **92**, 012911 (2008).
28. L. You, N. T. Chua, K. Yao, L. Chen, and J. Wang, *Phys. Rev. B* **80**, 024105 (2009).
29. Y. H. Chu, Q. Zhan, L. W. Martin, M. P. Cruz, P. L. Yang, G. W. Pabst, F. Zavaliche, S. Y. Yang, J. X. Zhang, L. Q. Chen, D. G. Schlom, I. N. Lin, T. B. Wu, and R. Ramesh, *Adv. Mater.* **18**, 2307 (2006).
30. G. P. Zhao, L. Chen, and J. Wang, *J. Appl. Phys.* **105**, 061601 (2009).
31. M. Stengel and N. A. Spaldin, *Nature* **443**, 679 (2006).
32. L. W. Chang, M. Alexe, J. F. Scott, and J. M. Gregg, *Adv. Mater.* **21**, 4911 (2009).
33. M. Stengel, D. Vanderbilt, and N. A. Spaldin, *Nat. Mater.* **8**, 392 (2009).
34. N. Balke, S. Choudhury, S. Jesse, M. Huijben, Y. H. Chu, A. P. Baddorf, L. Q. Chen, R. Ramesh and S. V. Kalinin, *Nature Nanotechnol.* **4**, 868 (2009).
35. H. Bea, M. Bibes, F. Ott, B. Dupe, X.-H. Zhu, S. Petit, S. Fusil, C. Deranlot, K. Bouzehouane, and A. Barthélemy, *Phys. Rev. Lett.* **100**, 017204 (2008)
36. J. G. Simmons, *J. Appl. Phys.* **34**, 1793 (1963).
37. H. Béa, M. Bibes, M. Sirena, G. Herranz, K. Bouzehouane, E. Jacquet, S. Fusil, P. Paruch, M. Dawber, J.-P. Contour, and A. Barthélemy, *Appl. Phys. Lett.* **88**, 062502 (2006).

- ³⁸. S. R. Basu, L. W. Martin, Y. H. Chu, M. Gajek, R. Ramesh, R. C. Rai, X. Xu, and J. L. Musfeldt, *Appl. Phys. Lett.* **92**, 091905 (2008).
- ³⁹. W. H. Butler, X.-G. Zhang, T. C. Schulthess and J. M. MacLaren, *Phys. Rev. B*, **63**, 054416 (2001).
- ⁴⁰. S. Yuasa, T. Nagahama, A. Fukushima, Y. Suzuki and K. Ando, *Nature Materials* **3**, 868 (2004).
- ⁴¹. S. V. Faleev, M. van Schilfgaarde, and T. Kotani, *Phys. Rev. Lett.* **93**, 126406 (2004);
M. van Schilfgaarde, T. Kotani, and S. V. Faleev, *Phys. Rev. Lett.* **96**, 226402 (2006);
T. Kotani, M. van Schilfgaarde, and S. V. Faleev, *Phys. Rev. B* **76**, 165106 (2007).
- ⁴². Mark van Schilfgaarde and M.I. Katsnelson, arXiv:1006.2426v1
- ⁴³. M. Shishkin, M. Marsman, and G. Kresse, *Phys. Rev. Lett.* **99**, 246403 (2007).
- ⁴⁴. S. Faleev, O. Mryasov and T. Mattsson, *Phys. Rev. B.*, **81**, 205436 (2010).
- ⁴⁵. J. B. Neaton, C. Ederer, U. V. Waghmare, N. A. Spaldin and K. M. Rabe, *Phys. Rev. B* **71**, 014113 (2005).
- ⁴⁶. C. Ederer and N. A. Spaldin, *Phys. Rev. Lett.* **95**, 257601 (2005).

CAPTION OF FIGURES:

- Fig 1** (a) The X-ray diffraction patterns for 100 (V119), 50 (V120), 20 (V121) and 10 (V122) nm BiFeO₃ films deposited with SrRuO₃ bottom layer on [110] vicinal SrTiO₃ substrates. Inset: Resolved (001) peaks.
Representative omega (b) and phi (c) scans to reveal crystalline and epitaxial nature.
- Fig 2** The surface topography scans (a)-(e) and corresponding ferroelectric domain structures (f)-(j) of 2 μm x 2 μm area of 100, 50, 20, 10 and 5 nm thickness BiFeO₃ films respectively.
- Fig 3** The variation of domain width as a function of film thickness for BFO films deposited on [110] vicinal substrates.
- Fig 4** Switching behavior of BFO films of variable thickness as revealed through SS-PFM: (a) amplitude, (b) phase, and (c) piezo-response signals as a function of tip bias.
- Fig 5** (a) Experimental J-V curve (black) and Simmons fit (red). The mean barrier height obtained is 4.15 eV (b) Simmons barrier model for 5nm BiFeO₃ film sandwiched between bottom SRO and Ir-Pt top electrode.
- Fig 6** The Electronic band structure of a) rhombohedral (R3c) and b) tetragonal (P4mm) phases of BiFeO₃ calculated along the high symmetry lines in Brillouin zone within the scaled QSGW (see text) (solid lines) and DFT-LDA (dash-dotted lines) theory. The F-Z line corresponds to measured direction of transport for the R3c phase.

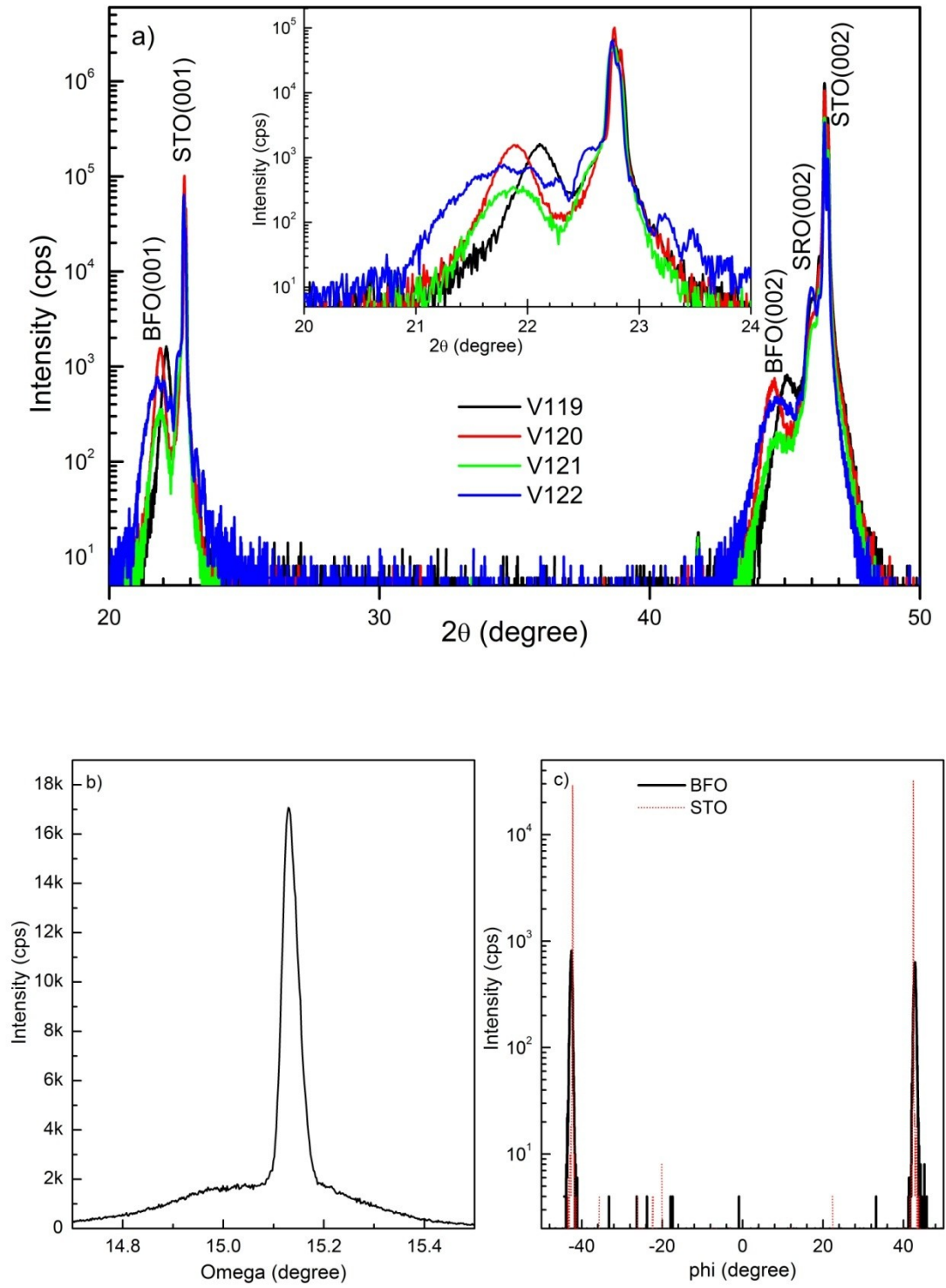


Fig. 1

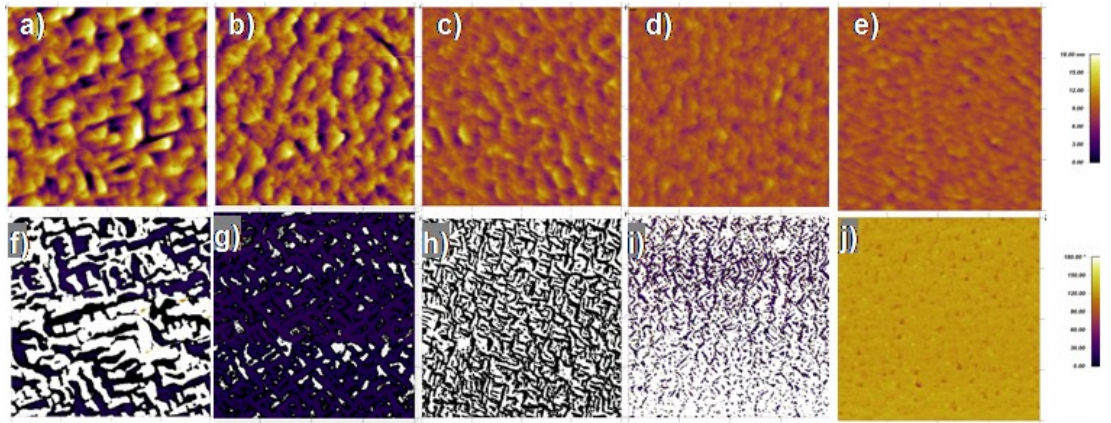


Fig 2

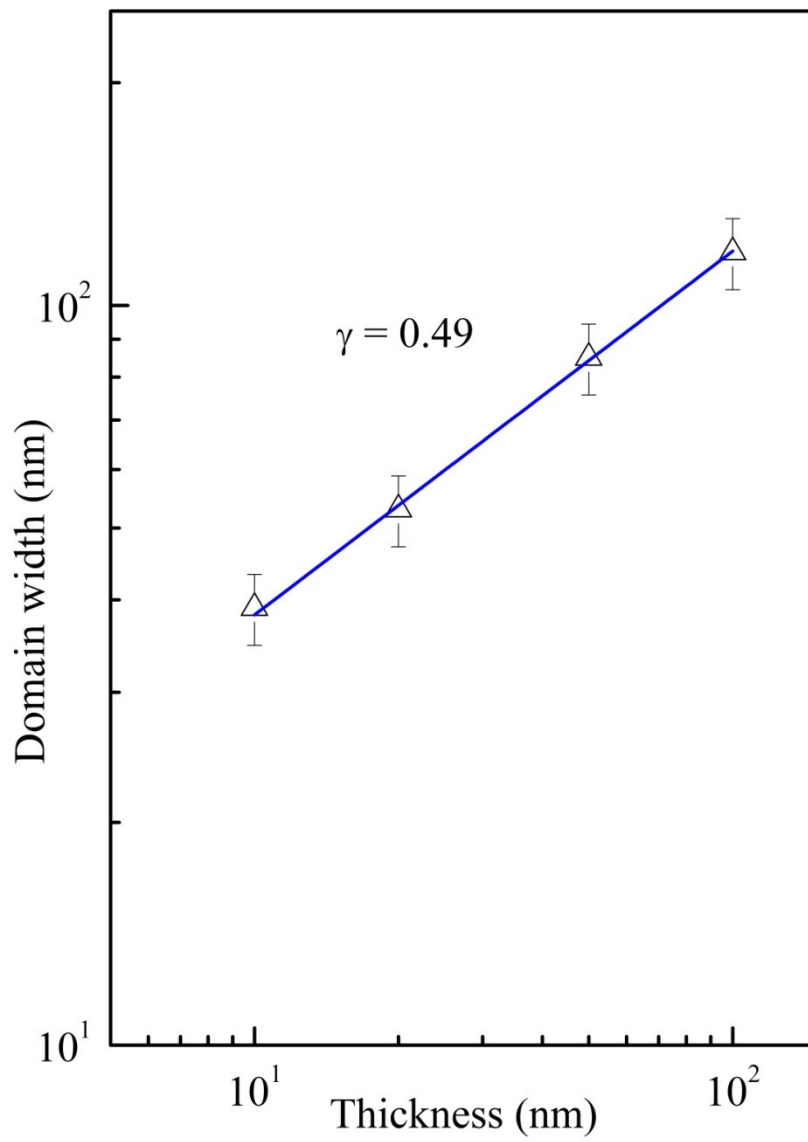


Fig 3

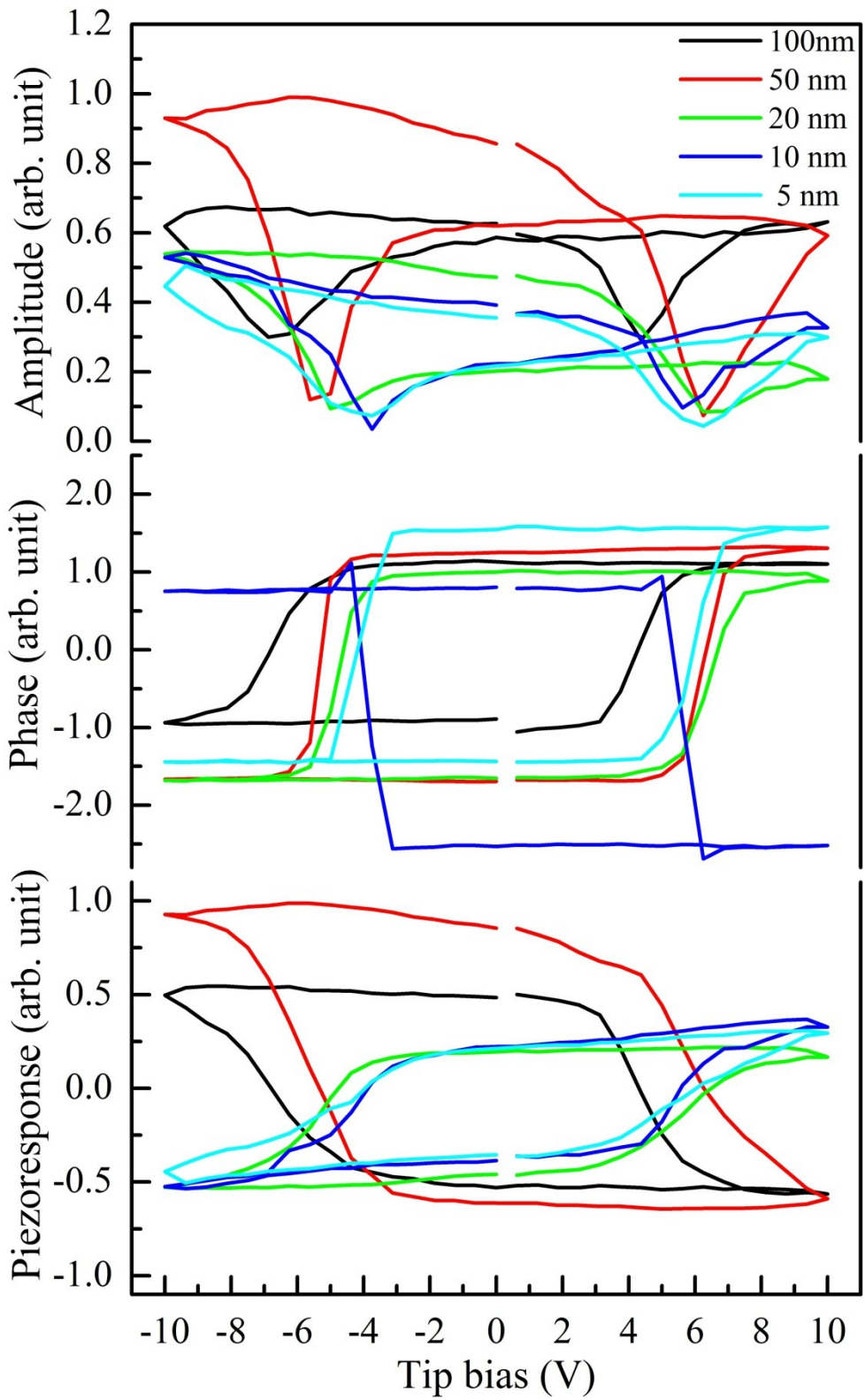


Fig 4

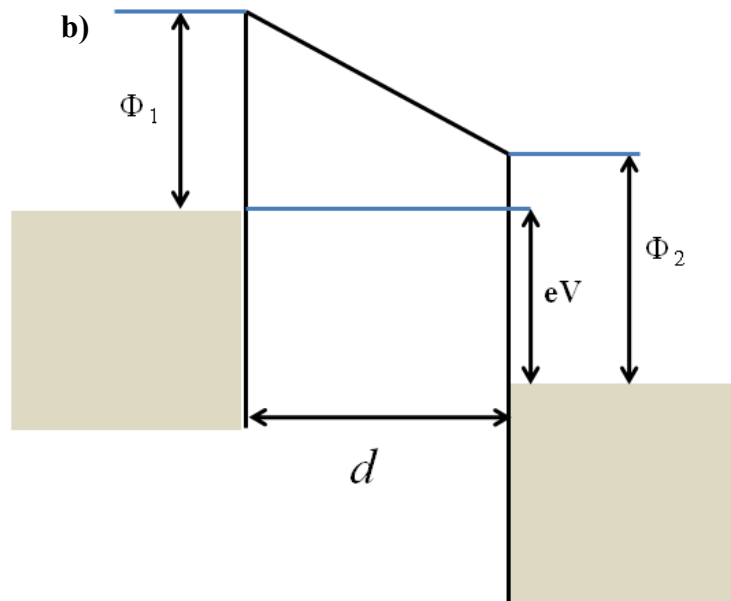
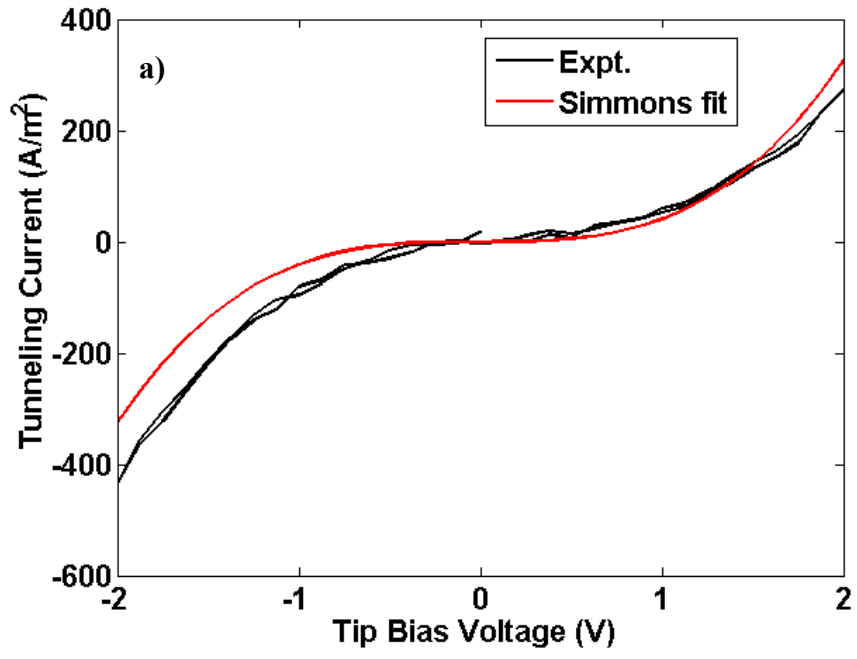


Fig 5

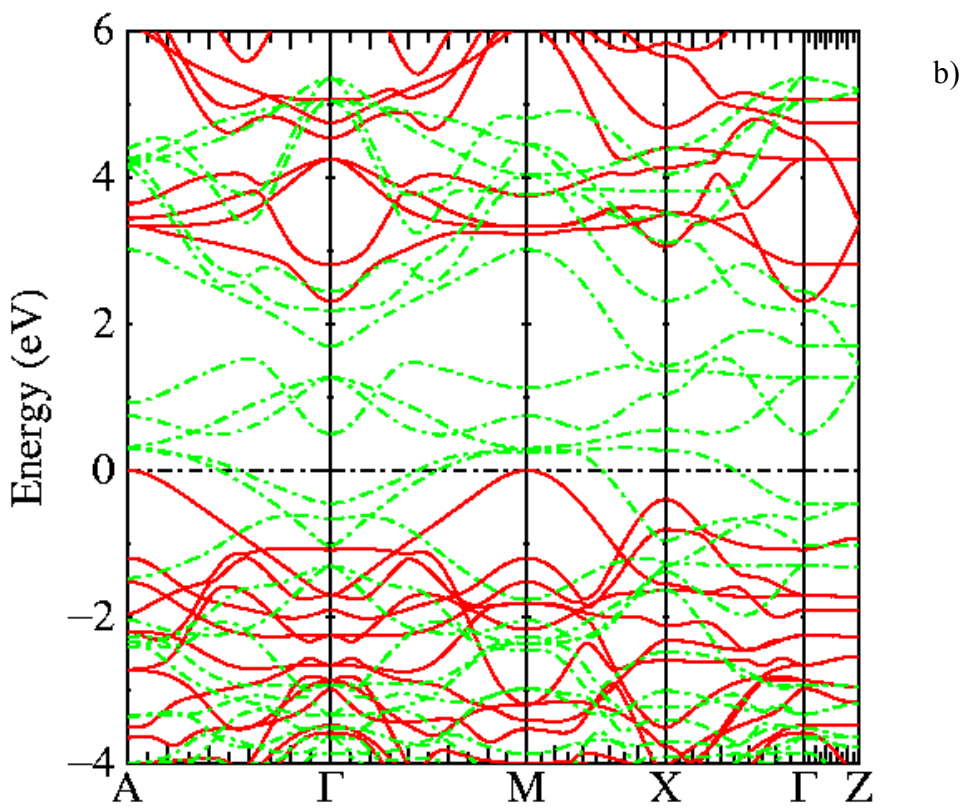
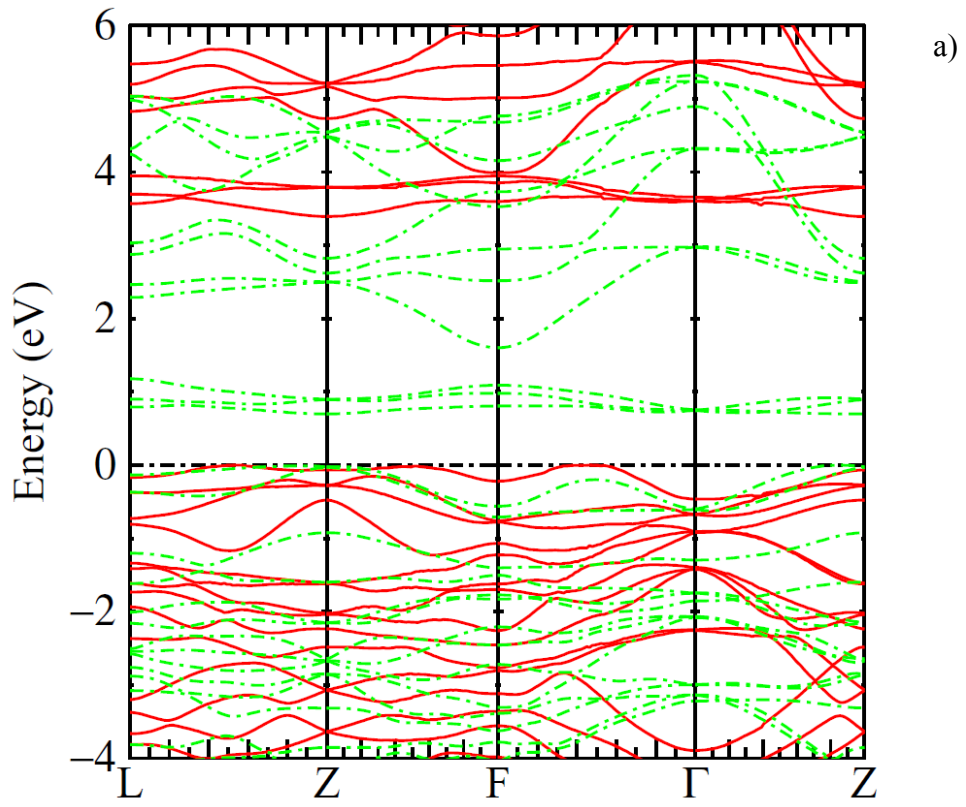


Fig 6